

This work was written as part of one of the author's official duties as an Employee of the United States Government and is therefore a work of the United States Government. In accordance with 17 U.S.C. 105, no copyright protection is available for such works under U.S. Law.

Public Domain Mark 1.0

<https://creativecommons.org/publicdomain/mark/1.0/>

Access to this work was provided by the University of Maryland, Baltimore County (UMBC) ScholarWorks@UMBC digital repository on the Maryland Shared Open Access (MD-SOAR) platform.

**Please provide feedback**

Please support the ScholarWorks@UMBC repository by emailing [scholarworks-group@umbc.edu](mailto:scholarworks-group@umbc.edu) and telling us what having access to this work means to you and why it's important to you. Thank you.

## Spectral discrimination of coarse and fine mode optical depth

N. T. O'Neill,<sup>1,2</sup> T. F. Eck,<sup>1,3</sup> A. Smirnov<sup>1,3</sup> B. N. Holben,<sup>1</sup> and S. Thulasiraman<sup>2</sup>

Received 24 September 2002; revised 11 March 2003; accepted 1 May 2003; published 12 September 2003.

[1] The recognition that the aerosol particle size distribution (PSD) is effectively bimodal permits the extraction of the fine and coarse mode optical depths ( $\tau_f$  and  $\tau_c$ ) from the spectral shape of the total aerosol optical depth ( $\tau_a = \tau_f + \tau_c$ ). This purely optical technique avoids intermediate computations of the PSD and yields a direct optical output that is commensurate in complexity with the spectral information content of  $\tau_a$ . The separation into  $\tau_f$  and  $\tau_c$  is a robust process and yields aerosol optical statistics, which are more intrinsic than those, obtained from a generic analysis of  $\tau_a$ . Partial (optical) validation is provided by (1) demonstrating the physical coherence of the simple model employed, (2) demonstrating that  $\tau_c$  variation is coherent with photographic evidence of thin cloud events and that  $\tau_f$  variation is coherent with photographic evidence of clear sky and haze events, and (3) showing that the retrieved values of  $\tau_f$  and  $\tau_c$  are well-correlated, if weakly biased, relative to formal inversions of combined solar extinction and sky radiance data. The spectral inversion technique permitted a closer scrutiny of a standard (temporally based) cloud-screening algorithm. Perturbations of monthly or longer-term statistics associated with passive or active shortcomings of operational cloud screening were inferred to be small to occasionally moderate over a sampling of cases. Diurnal illustrations were given where it was clear that such shortcomings can have a significant impact on the interpretation of specific events; (1) commission errors in  $\tau_f$  due to the exclusion of excessively high-frequency fine mode events and (2) omission errors in  $\tau_c$  due to the inclusion of insufficiently high-frequency thin homogeneous cloud events. **INDEX TERMS:** 0305 Atmospheric Composition and Structure: Aerosols and particles (0345, 4801); 0360 Atmospheric Composition and Structure: Transmission and scattering of radiation; 3360 Meteorology and Atmospheric Dynamics: Remote sensing; 4801 Oceanography: Biological and Chemical: Aerosols (0305); **KEYWORDS:** Sun photometry, aerosol, optical depth, fine mode, coarse mode, cloud screening

**Citation:** O'Neill, N. T., T. F. Eck, A. Smirnov, B. N. Holben, and S. Thulasiraman, Spectral discrimination of coarse and fine mode optical depth, *J. Geophys. Res.*, 108(D17), 4559, doi:10.1029/2002JD002975, 2003.

### 1. Introduction

[2] The aerosol optical depth ( $\tau_a$ ) and Angstrom exponent ( $\alpha = -\text{dln } \tau_a / \text{dln } \lambda$ ) are the workhorses of Sun photometry. The spectral derivative of the Angstrom exponent ( $\alpha' = \text{d}\alpha / \text{dln } \lambda$ ) yields significant aerosol optical information but arguably represents the practical spectral limits of operational Sun photometry [Eck *et al.*, 1999]. The essential optical effects of the aerosol particle size distribution (PSD) are largely bimodal and accordingly  $\tau_a$ ,  $\alpha$  and  $\alpha'$  can be expressed in terms of the analogous optical parameters of the component modes [O'Neill *et al.*, 2001a]. The simple

but fundamental relationships between the generic or total spectral parameters and the analogous spectral parameters of the component modes permit one to infer the optical properties of the fine and coarse mode components from an essentially spectral algorithm [O'Neill *et al.*, 2001b]. In this paper we will be concerned specifically with the extraction and analysis of the fine and coarse mode optical depths ( $\tau_f$  and  $\tau_c$  where  $\tau_a = \tau_f + \tau_c$ ). It is emphasized that these component optical depths are defined optically (rather than in terms of a microphysical cutoff of the associated particle size distribution at some specific radius) and essentially depend on the fact that the coarse mode spectral variation is approximately neutral [O'Neill *et al.*, 2001b].

[3]  $\tau_c$  is a measure of both coarse mode aerosols and thin cloud contamination (with the qualifier that in the presence of large particle cirrus clouds,  $\tau_c$  is systematically underestimated due to strong small angle scattering into the Sun photometer field of view; see Kinne *et al.* [1997]). Its value as deduced from the spectral algorithm (or "spectral inversion") thus provides indirect information on  $\tau_{\text{cloud}}$ . Current cloud screening algorithms typically employ exclusionary

<sup>1</sup>NASA Goddard Space Flight Center, Greenbelt, Maryland, USA.

<sup>2</sup>Now at Centre d'Applications et de Recherches en Télédétection, Université de Sherbrooke, Sherbrooke, Quebec, Canada.

<sup>3</sup>Also at Goddard Earth Sciences and Technology Center, University of Maryland Baltimore County, Baltimore, Maryland, USA.

constraints based on the principle that large temporal variations in  $\tau_a$  are induced by variations in  $\tau_{\text{cloud}}$ . These latter algorithms thus embody temporal information on the variability of  $\tau_{\text{cloud}}$  which complements the  $\tau_c$  information provided by the spectral algorithm employed in this paper.

[4] If fine and coarse mode PSDs can be viewed as physically separate entities then it stands to reason that the optical characterization of aerosols by Sun photometry should incorporate a standard and robust segmentation into fine and coarse mode optics. This capability is, for example, a validation requirement of the MODIS sensor whose aerosol products include the ratio  $\eta$  of fine to total aerosol optical depth [Tanré *et al.*, 1999]. Sun photometry is also an important tool in validating aerosol models of local, regional or global extent; comparisons between model and measurement cannot be adequately understood if the optical measurements and model estimates of these measurements are not segmented into their more fundamental components.

[5] Such segmentation is in actual fact carried out by the AERONET group but only for the comparatively complex and relatively infrequent cases involving the inversion of combined Sun photometry and sky radiometry data [Dubovik *et al.*, 2002]. Depending on one's objectives this approach unnecessarily bypasses the more simplistic option of a pure extinction analysis since any spectral extinction measurement involving at least four strategically placed bands can be processed to discriminate fine and coarse mode information at a level of algorithmic sophistication which is commensurate with the simplicity of the essentially bimodal optical mechanisms.

[6] The objective of this paper is to optically validate the extraction of  $\tau_f$  and  $\tau_c$  obtained from the spectral curvature algorithm. This will be accomplished by (1) demonstrating the physical consistency of the bimodal optical formulation and the component extractions, (2) by qualitatively demonstrating a link between  $\tau_c$  and the presence of cloud as well as  $\tau_f$  and the presence of haze and (3) comparing the simple spectral inversion technique with formal inversions of solar extinction and sky radiance data. Because this validation is partial in that it is limited to the optical domain (and does not include, for example, independent and simultaneously acquired measurements of microphysical aerosol parameters) it is perhaps better described as a verification of optical coherency between model and measurement.

## 2. Methodological Considerations

### 2.1. Theoretical Background

#### 2.1.1. Spectral Curvature Relations

[7] The total optical curvature parameters,  $\tau_a$ ,  $\alpha$ , and  $\alpha'$  characterize most of the variability in the aerosol optical depth spectra [Eck *et al.*, 1999] and are intimately related with analogous parameters characterizing the fine and coarse mode components of the bimodal PSD [O'Neill *et al.*, 2001a]. In this paper the three parameters are all derived at a reference wavelength of 500 nm from a second-order polynomial fit of  $\ln \tau_a$  versus  $\ln \lambda$  applied to each measured  $\tau_a$  spectrum (across 6 bands at 380, 440, 500, 670, 870 and 1020 nm). It should be clear that the use of a polynomial means we are mathematically free to derive any spectral derivative at the nominal value of 500 nm. In order to avoid a burdensome and redundant nomenclature, the 500 nm

**Table 1.** Analytical Expressions for Fine and Coarse Mode Events

Fine Mode Event <sup>a</sup>	Coarse Mode Event <sup>b</sup>
$\alpha = \alpha_f - \frac{a_c}{\tau_a}$	$\alpha = \alpha_c + \frac{a_f}{\tau_a}$
$\alpha' - \alpha'_{\min} = c_c \left( \frac{1}{\tau_a} - \frac{b_c}{2c_c} \right)^2$	$\alpha' - \alpha'_{\min} = c_f \left( \frac{1}{\tau_a} - \frac{b_f}{2c_f} \right)^2$
$\alpha' - \alpha'_{\min} = (\alpha - \alpha_f + \frac{b_c}{2a_c})^2$	$\alpha' - \alpha'_{\min} = (\alpha - \alpha_c + \frac{b_f}{2a_f})^2$
<i>Constants<sup>c</sup></i>	
$a_c = (\alpha_f - \alpha_c)\tau_c, c_c = a_c^2$	$a_f = (\alpha_f - \alpha_c)\tau_f, c_f = a_f^2$
$b_c = [\alpha_f' - \alpha_c' + (\alpha_f - \alpha_c)^2]\tau_c$	$b_f = [\alpha_f' - \alpha_c' + (\alpha_f - \alpha_c)^2]\tau_f$
$\alpha'_{\min} = \alpha_f' - \frac{b_c^2}{4c_c}$	$\alpha'_{\min} = \alpha_c' - \left( \frac{b_f}{2c_f} \right)^2$
$\alpha_f = a\alpha_f^2 + b\alpha_f + c$	$\alpha_c = a\alpha_c^2 + b\alpha_c + c$

<sup>a</sup>Fine mode event with variable  $\alpha_f$  ( $\tau_c = \text{constant}$  with either (1)  $\alpha_f = \text{constant}$  or (2) variable  $\alpha_f$  where  $d\alpha_f/d\log\tau_a = \text{constant} = -d$ ). For the variable  $\alpha_f$  case,  $\alpha_f = -d(\log\tau_a + 1) + \alpha_f(1)$ .

<sup>b</sup>Where  $\tau_c$  is constant.

<sup>c</sup>Where a, b, and c of the last equation are given by O'Neill *et al.* [2001b].

reference wavelength is not written explicitly in this paper (i.e.,  $\tau_a = \tau_a(500 \text{ nm})$ ,  $\alpha = \alpha(500 \text{ nm})$ ,  $\alpha' = \alpha'(500 \text{ nm})$ ,  $\tau_f = \tau_f(500 \text{ nm})$ ,  $\tau_c = \tau_c(500 \text{ nm})$ , etc.). The specific use of a second-order polynomial is a modification to the original employment of a third-order polynomial [O'Neill *et al.*, 2001a] since it was felt that, in an operational setting, the benefits of noise filtering offered by the former outweigh the increased spectral responsivity of the latter.

[8] The total optical parameters can be employed to extract optical information on the separate components of the bimodal distribution. The fundamental equations for the derivation of the fine mode Angstrom exponent ( $\alpha_f$ ) from the total optical parameters are given in O'Neill *et al.* [2001b]. The ratio  $\eta$  and the individual optical depths can then be computed, namely

$$\eta = \frac{\tau_f}{\tau_a} = \frac{\{\alpha - \alpha_c\}}{\{\alpha_f - \alpha_c\}} \quad (1a)$$

$$\tau_f = \eta\tau_a \quad (1b)$$

$$\tau_c = \tau_a - \tau_f. \quad (1c)$$

#### 2.1.2. Optical Behavior for Different Types of Events

[9] Atmospheric optical events are typically dominated by particle number changes in the fine or coarse mode PSD. In the simplest conceptual model, one can look for approximations to pure fine mode events ( $\tau_c = \text{constant}$ ) or pure coarse mode events ( $\tau_f = \text{constant}$ ) with the component curvature parameters ( $\alpha_f$ ,  $\alpha_f'$ ,  $\alpha_c$ ,  $\alpha_c'$ ) being roughly constant. Table 1 is a compilation of the analytical equations expected for the total optical parameters of  $\tau_a$ ,  $\alpha$  and  $\alpha'$  assuming the pure fine mode and pure coarse mode conditions, respectively (these equations were derived from the basic bimodal expressions given by O'Neill *et al.* [2001a]). Figure 1 shows an application of these equations superimposed on two data sets representing coarse and fine mode events. The families of analytical curves represent pure fine mode events (convex upward) and pure coarse mode events (convex downward). An added parameterization in the case of the fine mode analytical curves is the assumption that the effective radius of fine mode particles increases with in-

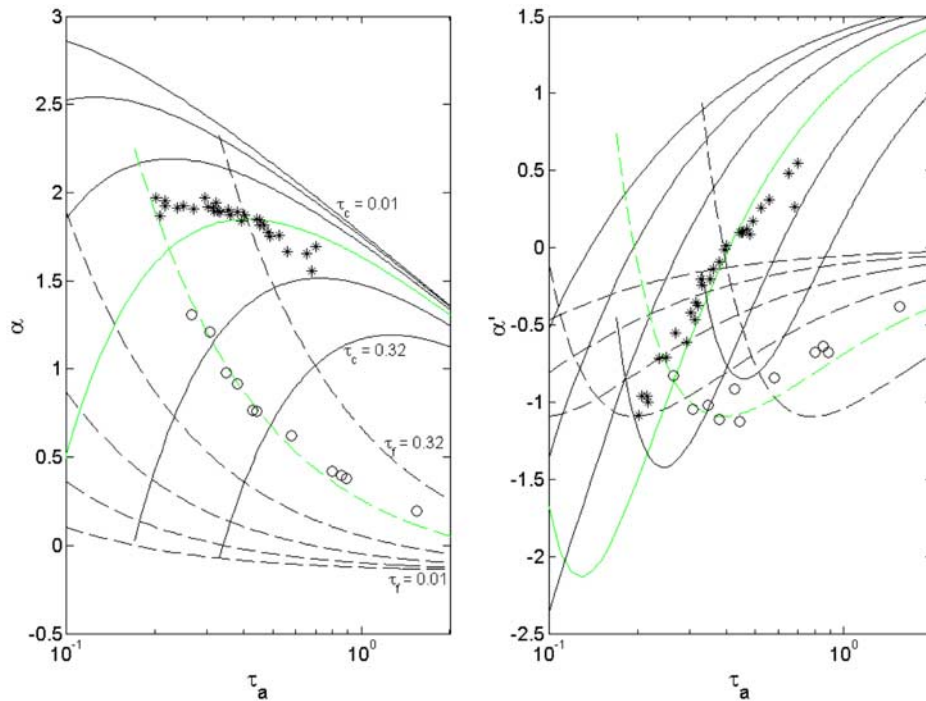


**Figure 1.** Spectral curvature variation of the total optical parameters for a typical coarse mode event (open circles) and a typical fine mode event (asterisks). These data were acquired on 11 and 27 June 2001, respectively, at the CARTEL site in Sherbrooke, Quebec, Canada. The black curves represent families of analytical approximations;  $\tau_f = \text{constant}$  for the coarse mode event and  $\tau_c = \text{constant}$ ,  $d\alpha_f/d\log \tau_a = \text{constant}$  for the fine mode event (produced using the equations of Table 1). The green-colored curves represent the analytical fit nearest to the data points.

creasing  $\tau_a$  or equivalently that  $\alpha_f$  decreases with increasing  $\tau_a$  [Eck *et al.*, 1999; O'Neill *et al.*, 2001a]. The green curves highlight the analytical curve, which most closely resembles the variation of the two illustrative data sets. The constants of the most representative analytical curve ( $a_x$ ,  $b_x$  and  $c_x$  of Table 1) were set to realistic values of the fine and/or coarse mode parameters which would have occurred during the measuring period. Our objective in displaying these total optical parameter curves is to illustrate that measurement trends in the total parameters can be approximately coherent with specific analytical cases derived from the bimodal relationships and accordingly that the bimodal equations are realistic representations of nature. Given these types of trends one can also readily appreciate how the spectral inversions often yield approximately pure fine mode events or pure coarse mode events.

## 2.2. Instrumentation and Data Processing

[10] Aerosol optical depth spectra were acquired by automated CIMEL Sun photometer/sky radiometers belonging to the AERONET and/or AEROCAN network (the AEROCAN network is a Canadian subnetwork of AERONET). In solar extinction mode the CIMEL operates in seven spectral bands (340, 380, 440, 500, 675, 870 and 1020 nm plus a 940 nm water vapor band; 10 nm full width at half maximum band pass, except 4 and 2 nm, respectively, for the 340 and 380 nm bands) and in sky radiance mode it scans off the solar disk to acquire directional distributions of sky radiance data at four wavelengths (440, 675, 870 and 1020 nm). Details

concerning the operations and data processing logistics of this network are given by Holben *et al.* [1998].

[11] The spectral curvature inversion algorithm employed in this work is based on the solar extinction data (excluding the 340 nm band from the seven bands given above since this band is typically more susceptible to errors than the other bands). Since the algorithm amounts to a partial cloud screening technique it is typically applied to pre cloud-screened (level 1.0) data although it can be equally well applied to cloud-screened data. The cloud-screened data are an operational (level 1.5) output product of the AERONET processing chain [Smirnov *et al.*, 2000]. The AERONET cloud screening process principally involves temporal smoothing constraints applied to optical depth variations. If available, we preferentially employed level 2.0 (cloud screened and QA'd) data rather than level 1.5 data (when we were comparing cloud screened data with non cloud-screened data). This latter data set is monitored for anomalous instrumental artifacts and is re-calibrated using calibration coefficients derived before and after the period of observation.

[12] Formal inversions of extinction and sky radiance [Dubovik and King, 2000] are employed in this paper as a means of optically validating the estimations of the spectral inversion algorithm. It is important to note that the latter data set is distinct from the solar extinction data set and is updated at relatively infrequent intervals. A qualitative but objective assessment of sky conditions is provided by total sky images acquired by Yankee Environmental Systems

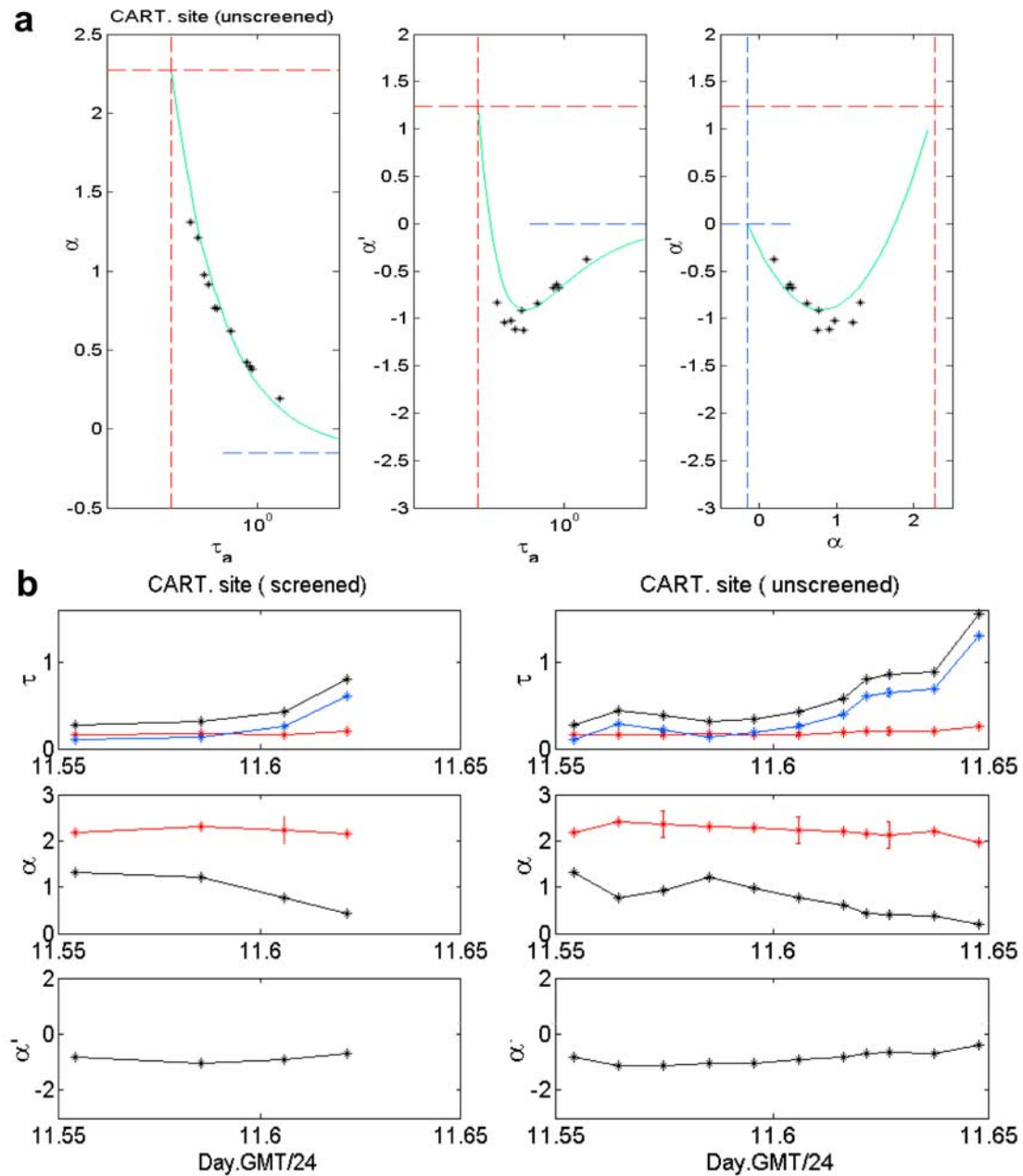


**Figure 2.** Total and spectrally derived optical parameters for the thin homogeneous cloud event of Figure 1. (a) Interrelationship of total 500 nm optical parameters (green curves represent the analytical form of the coarse mode event for  $\tau_f = \text{constant}$ ). The colored lines (red for fine mode and blue for coarse mode) represent mean values of fine and coarse mode parameters observed in the temporal profile curves. The green curves were produced using the analytical forms given by the  $\tau_f = \text{constant}$  equations of Table 1 (with the “constants” of the most representative analytical curve being obtained from averages of the fine and/or coarse mode parameters extracted from the spectral inversion over the duration of the measuring period). (b) Temporal profile of total, and derived fine and coarse mode (500 nm) parameters (black, red, and blue curves, respectively). The left hand set of figures is for cloud-screened data while the right hand set of figures is for non cloud-screened data (11.5 means 11 June, GMT noon).



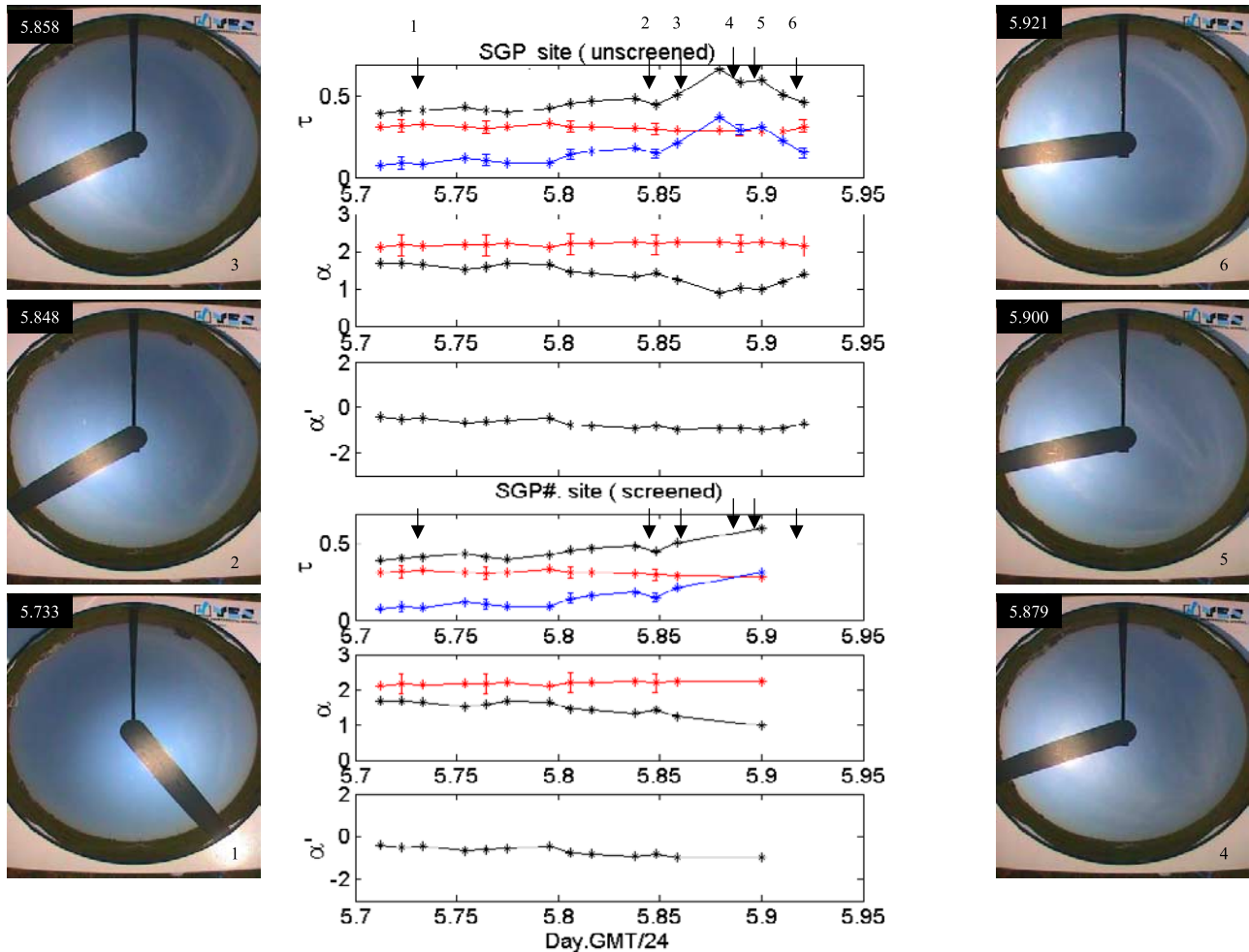


**Figure 3.** Spectral curvature inversion applied to non cloud-screened data (top curves) and cloud-screened data (bottom curves) during a thin homogeneous cloud event at the southern Great Plains, Oklahoma, AERONET site on 5 August 2000. The timescale shows the date followed by the fraction of the day in GMT after the decimal point (5.5 means 5 August, GMT noon). Sky images (arranged sequentially from top to bottom and left to right) are from the YES sky imager located at that site. The arrows at the top of the temporal plots indicate the approximate acquisition time of the sky images.

(YES) sky imagers at the Egbert, Ontario, AEROCAN site and the southern Great Plains AERONET site.

### 3. Validation of the Spectral Inversion Algorithm

#### 3.1. Coherency of Retrievals and Comparisons With Sky Imagery

##### 3.1.1. Thin Homogeneous Cloud Events

[13] Figure 2 shows an example of a slowly thickening, homogeneous, cirrus like veil witnessed by one of the authors. The top set of three graphs show the intercorrelation of the total optical parameters (including the analytical  $\tau_f = \text{constant}$  approximation in green) while the bottom set of graphs show the temporal behavior of the total (black curves) and derived optical curvature parameters for non cloud-screened and cloud-screened data (red and blue for fine and coarse modes, respectively). The error bars (taken only every 3 points to avoid clutter) were generated by the error model presented below. Taken as a whole the curves demonstrate the consistency of the bimodal formulation and the spectral curvature inversion algorithm in terms of a

number of interrelated attributes; (1) the fine mode parameters remain relatively constant as one would expect for a thin cloud event superimposed on a stable fine mode background, (2) the coarse mode (cloud) optical depth mimics the temporal behavior of the total optical depth and (3) the interdependency of the total parameters is well modeled by the analytical curves of Table 1.

[14] A thin homogeneous cloud event which occurred at the southern Great Plains AERONET site can be seen in the post 19:00 GMT (post 5.8) sky images of Figure 3. Correspondingly, the values of  $\tau_c$  are seen to increase while  $\tau_f$  remains relatively constant. If one accepts this as qualitative proof that  $\tau_c$  is a realistic indicator of cloud presence then the bottom (cloud-screened) sets of curves indicate that, while some of the cloud points were rejected, a sizable fraction were retained (6 out of 10). There is, in actual fact, no surprise in this latter result since the strategy of the AERONET cloud screening was liberal; to interfere as little as possible with coarse mode events such as dust incursions and thus to accept the inevitability of some thin homogeneous cloud data being admitted into the database. It is clear

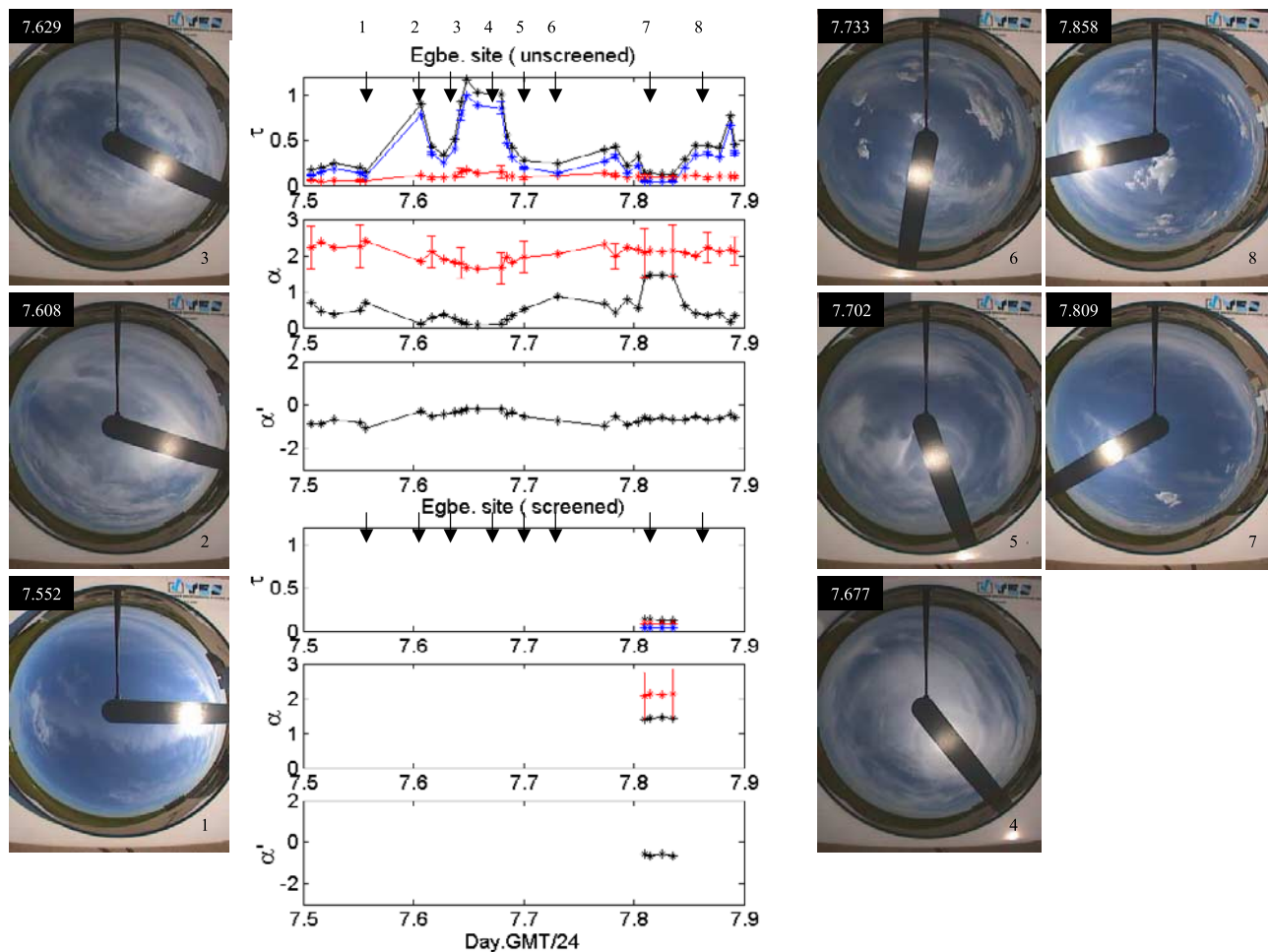


**Figure 4.** Spectral inversion applied to non cloud-screened data (top curves) and cloud-screened data (bottom curves) during a thin cloud event at Egbert, Ontario, on 7 June 2001. See Figure 3 for a key.

that the temporal behavior of  $\tau_c$  helps to infer when such contaminations occur.

### 3.1.2. Thin Inhomogeneous Cloud Event

[15] In Figure 4 we see a good example of a nonhomogeneous thin cloud event at the Egbert, Ontario, AEROCAN site. Peaks and valleys in the variation of the non cloud-screened values of  $\tau_a$  and  $\tau_c$  correspond qualitatively with the sky images while the value of  $\tau_f$  remains relatively small and constant. The presence of high cirrus is suggested by the halo which can be seen in the sky images at the labeled times of 7.677 and 7.702. One can also observe that the AERONET cloud-screening procedure has met its design requirements and eliminated all but four points around 19:30 GMT (7.82). Coincidentally, one notes the physical consistency of the spectral curvature algorithm inasmuch as  $\tau_c < \tau_f$  only within this small time window (i.e., implying that  $\tau_c \sim \tau_{\text{cloud}}$  outside this window and that  $\tau_c$  is associated with coarse mode aerosols inside the window).

### 3.1.3. Fine Mode Pollution Event

[16] Temporal variations and sky images for a fine mode pollution event can be seen in Figure 5 (the cloud-screened graphs are not shown because these graphs are virtually identical to the non cloud-screened graphs). The spectral inversion algorithm is again coherent with expectations and

yields values of  $\tau_f$  which are essentially superimposed on  $\tau_a$  while the values of  $\tau_c$  are indistinguishable from zero. That little or no information on  $\tau_c$  is available under such conditions is predicted by the error model and is understandable given the fact that the error in the estimated value of  $\eta$  (mostly due to the uncertainty in  $\alpha'_f$  and  $\alpha'_c$ ) was  $\sim 10\%$ . This translates into an error  $\sim 0.1$  in optical depth (i.e., significantly greater than the value of  $\tau_c$  which one typically finds in atmospheres unperturbed by coarse mode events). The sky photos are correspondingly hazy in appearance (compare these with the low  $\tau_f$  and  $\tau_c$  sky photo labeled 7.809 during the short clear sky time period of Figure 4).

### 3.2. Comparison With Microphysical Inversions

[17] Figures 6a, 6b, and 6c show the temporal correlation obtained between estimates of  $\tau_f$  and  $\tau_c$  from the spectral inversion compared with those obtained from the spectral extinction and sky radiance inversion of *Dubovik and King* [2000]. The data are not cloud-screened in the operational AERONET sense but rather represent samples that passed the screening filter applied to inversion data (this implies scan symmetry criteria and the existence of smooth sky radiance distributions in addition to the added constraints given in the caption to Figure 6). Figure 6a represents predominantly fine mode events at Egbert, Ontario, while Figure 6b shows

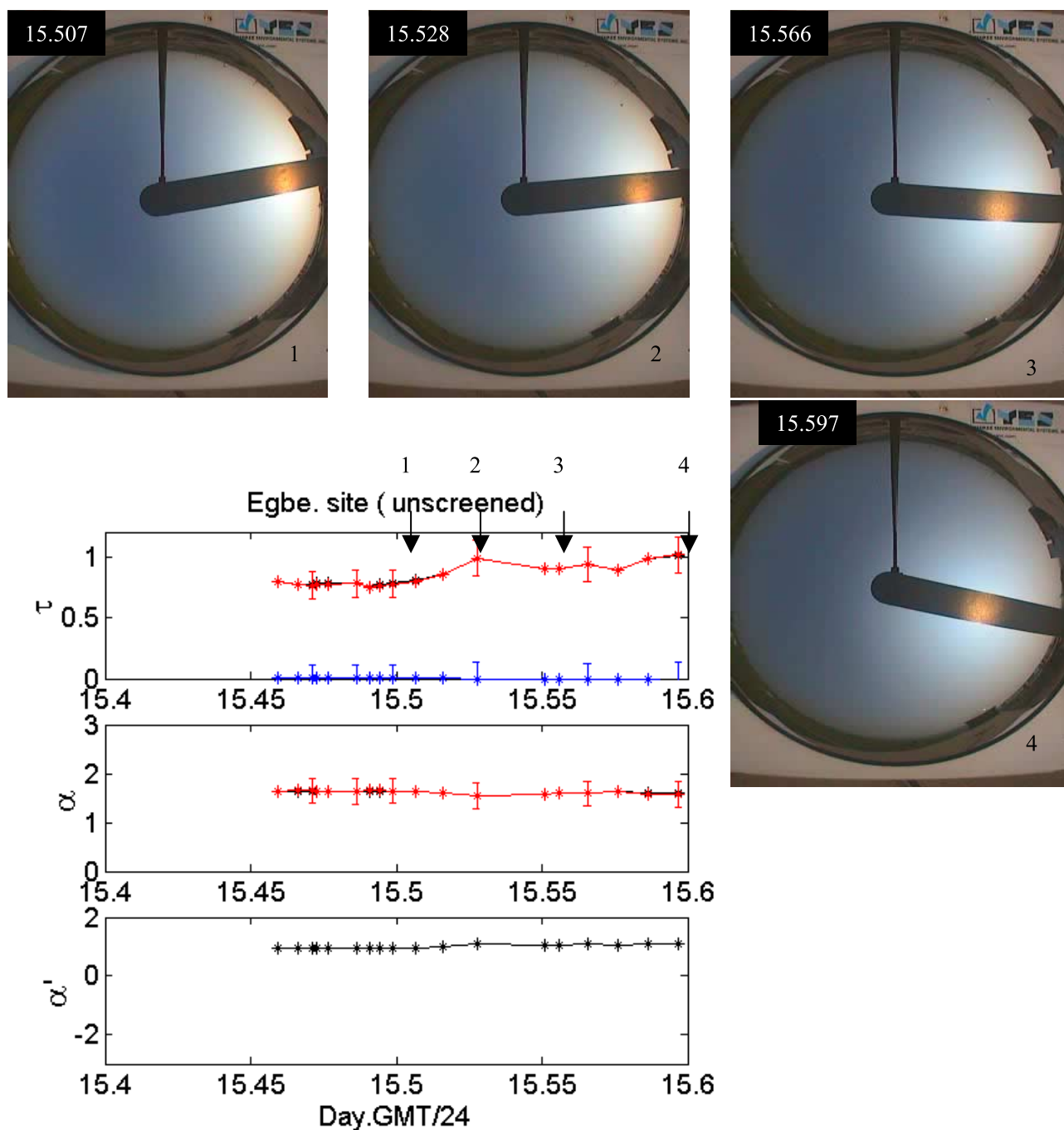


**Figure 5.** Spectral inversion applied to non cloud-screened data during a fine mode pollution event at Egbert, Ontario, on 15 June 2001. See Figure 3 for a key.

comparisons during heavy dust loading at the AERONET Bahrain site on the Persian Gulf. Figure 6c represents an interesting ten day period at GSFC Maryland which included a strong fine mode pollution event in the early part of May as well as possible dust loading event in the latter part of April (due to the spring 2001 Asian dust storms).

[18] In general the correlation is strong while suffering from a negative bias in  $\tau_f$  and a corresponding positive bias in  $\tau_c$ . The amplitude of the bias is small but its persistence merits attention (the average  $\tau_c$  bias for each case of Figure 6 ranges from 0.015 to 0.03 and is somewhat dependent on the magnitude of  $\tau_c$ ). One potential source

of this bias can be ascribed to the definition of fine and coarse mode optical depth. The spectral curvature algorithm defines these two parameters optically (essentially by exploiting the neutral curvature of coarse mode particles) while the current AERONET processing algorithm defines the parameters by the simple expedient of dividing the PSD into two at  $0.6 \mu\text{m}$  and then recalculating the optics from the two halves. If one assumes that the fine and coarse particles PSDs are continuous entities which spread beyond the borders of the  $0.6 \mu\text{m}$  cutoff then an imbalance is created because the Mie kernel of the optical integrations over particle size weights the missing sub  $0.6 \mu\text{m}$  half



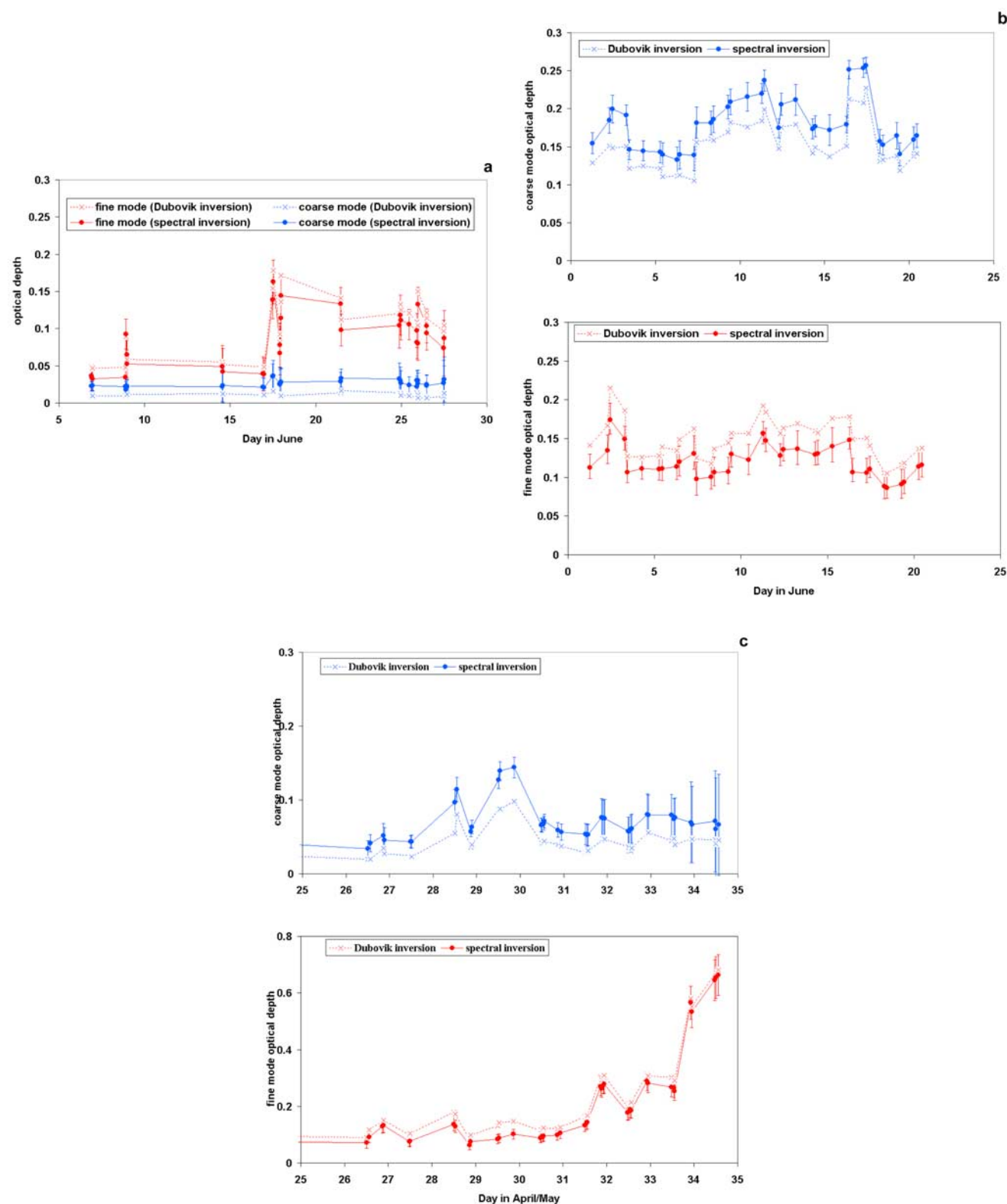


**Figure 6.** Spectral curvature inversion versus the Dubovik inversion. For GSFC and Egbert the scan/inversion constraints were a solar zenith angle (SZA)  $>45^\circ$ , relative inversion residuals  $<0.05$ , application of the AERONET level 2.0 quality control criteria and elimination of inversions for which the size distribution of the largest or smallest radii bins was labeled as abnormally large. Similar constraints were employed for the Bahrain data except the SZA was limited to values between  $25^\circ$  and  $45^\circ$  (to minimize particle nonsphericity effects). (a) Egbert during the month of June 2001. (b) Bahrain during the month of June 1999. (c) GSFC for 10 days during the end of April and the beginning of May 2001.

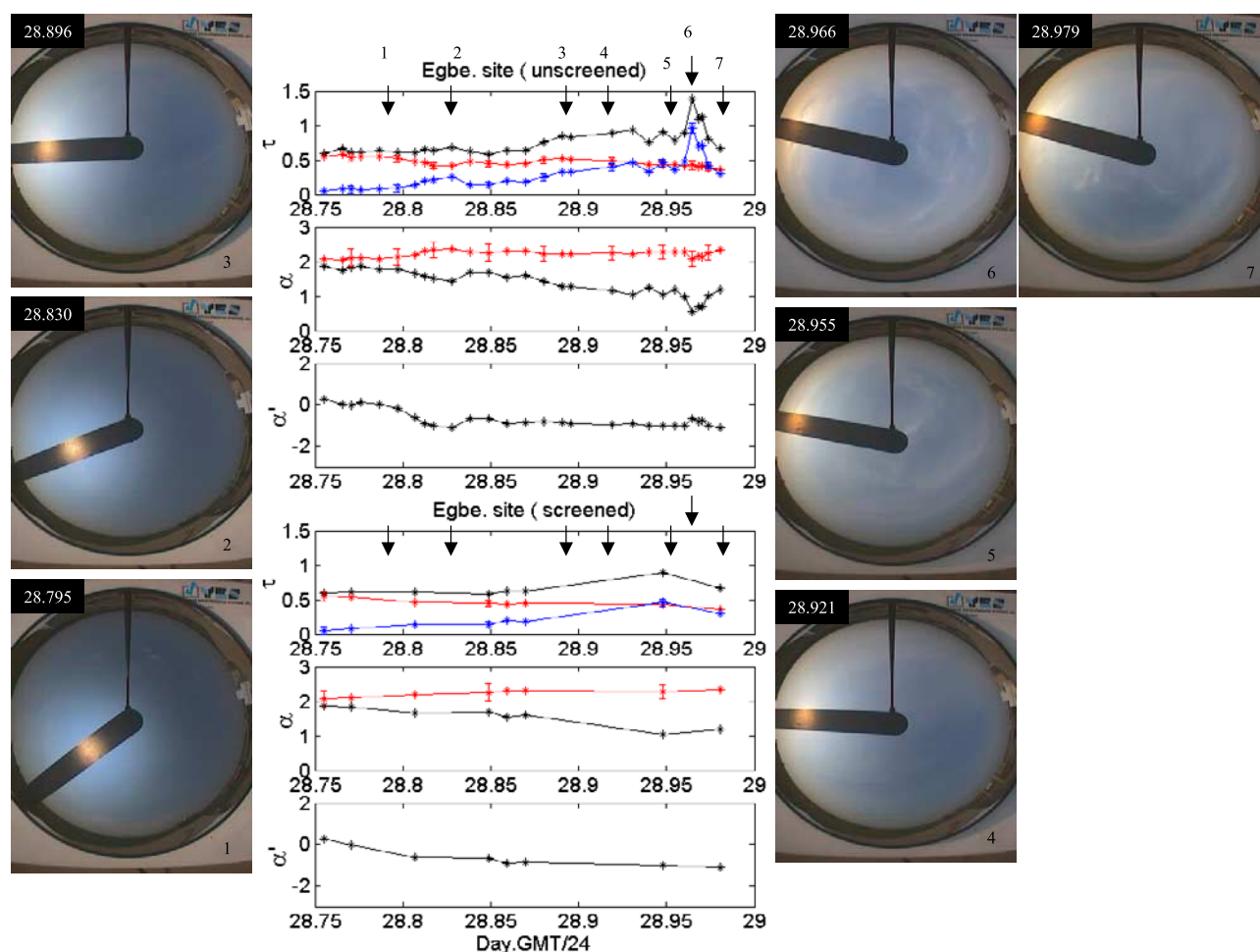


**Figure 7.** Spectral inversion applied to cloud-screened and non cloud-screened data for 28 June 2001 at the Egbert site (mixed mode event). See Figures 2 and 3 for a key.

significantly more heavily than the missing super  $0.6 \mu\text{m}$  half (the truncation effect is significantly more important on the coarse mode extension into the fine mode region). It is easy to demonstrate that, for the Dubovik inversion,  $\tau_c$  will typically be underestimated and  $\tau_f$  overestimated by a small amount, which is a significant portion of biases, observed in Figure 6. We cannot however exclude other potential sources of bias generated by the assumptions in the spectral curvature algorithm (see the error section below).

#### 4. Spectral Discrimination Versus Temporal Cloud Screening

[19] Both the spectral curvature inversion algorithm and the standard AERONET cloud-screening algorithm provide information on the contribution of aerosols and clouds to solar beam extinction. The complementarity of this information is investigated in the illustrations of the following sections.

##### 4.1. Other Diurnal Examples

[20] Figure 7 illustrates a mix of fine mode, thin homogeneous cloud and thin inhomogeneous cloud events. The spectral curvature inversion again appears to capture the

cloud events while the AERONET cloud screening (as in Figure 4) eliminates the inhomogeneous portion (the peak around 28.97) and retains some of the points in the homogeneous portions. Figure 8 shows a very strong smoke event due to the northern Quebec forest fires of July 2002. In this case, cloud screening acts to remove 90% of the data acquired during the 6 July smoke event at Egbert while the spectral curvature algorithm retains all measurements and appropriately indicates a fine mode event.

##### 4.2. Statistical Considerations

[21] It is clear that  $\tau_a$  statistics will yield a less intrinsic version of an analysis that incorporates the separate statistics of  $\tau_f$  and  $\tau_c$ . In this section we give examples of such statistics in order to illustrate the relevance of fine and coarse mode discrimination and to better appreciate the coupling between temporal based cloud screening and spectral discrimination.

[22] Figure 9 is a sampling of AERONET histograms for non cloud-screened and cloud screened ensembles of  $\tau_a$ ,  $\tau_f$  and  $\tau_c$ . The number of measurements differs between each type of optical depth ensemble since marginal values have been eliminated in the case of the derived optical depths (optical depths < an assumed nominal noise value of 0.01

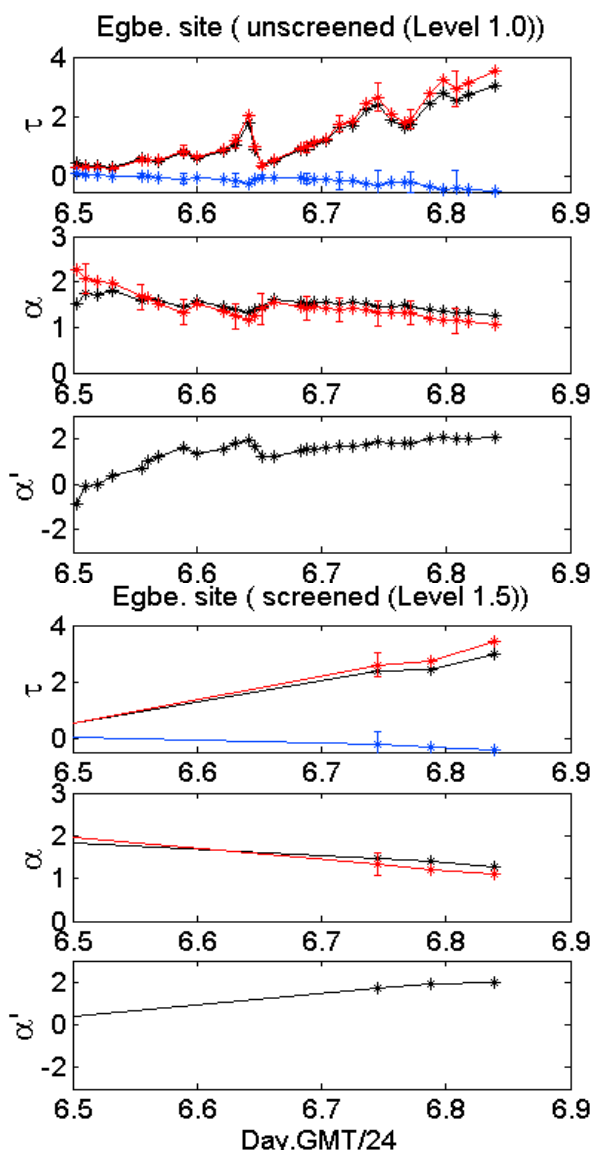


**Figure 8.** Spectral inversion applied to cloud-screened and non cloud-screened data for 6 July 2001 at the Egbert site (heavy smoke). See Figures 2 and 3 for a key.

and for which the estimated  $S/N < 1$ ). Figure 9a shows the total and separated statistics of Bahrain during the (dust laden) month of June 1999. This is a germane illustration which suggests the importance of separating physically distinct modes and which demonstrates the (appropriately) weak interference of the AERONET cloud screening in the presence of strong but relatively homogeneous  $\tau_c$ .

[23] Figure 9b shows the statistics of the Egbert site for the month of June 2001 (the month from which the illustrations above were taken). The appearance of the  $\tau_c$  histogram before and after cloud-screening effectively confirms the apparent efficiency of the AERONET cloud-screening algorithm inasmuch as the asymmetric (large  $\tau_c$ ) tail is largely eliminated. At the same time a significant fraction of  $\tau_f$  measurements are unnecessarily eliminated

(with a minor but systematic influence on the  $\tau_f$  statistics) and a remnant of an asymmetric  $\tau_c$  tail can still be observed. The larger  $\tau_c$  measurements ( $\sim 0.06$  and greater) are unlikely to be aerosol in nature since there are ordinarily no strong sources of coarse mode aerosol for such sites (the value of 0.06 is suggested from previous statistics generated using the Dubovik inversion [O'Neill et al., 2001b]). Also, it can be demonstrated that these larger  $\tau_c$  values are often associated with high-frequency temporal changes (but which are not of sufficiently high frequency to be caught by the AERONET cloud screening).

[24] Figure 9c shows the statistics for the GSFC site during the month of July 2002. This particular month was affected by extraordinarily strong fine mode pollution events as well as the Quebec smoke event of 2002. Cloud screening induces a strong depletion of the histograms and (if one accepts the hypothesis that the non cloud-screened  $\tau_f$  histogram is a realistic interpretation of nature) a moderate underestimate in the geometric mean of  $\tau_f$ .

[25] Figure 9d is a compilation of annual statistics (1 June 1999 to 31 May 2000) for the Nauru, Pacific Ocean site which has served as a key station for studies of the maritime aerosol [Smirnov et al., 2002]. Although the relative  $\tau_f$  and  $\tau_c$  errors were large for this low optical depth site the large-sample statistics appear to be stable. In particular one can note the extraordinarily small geometric mean value of  $\tau_f$  which is near or slightly larger than the values reported by [Kent et al., 1994] for the combined contributions of upper tropospheric and stratospheric aerosols.

## 5. Error Estimation

[26] The retrieval error bars seen in the previous figures were computed from a differential error model composed of incoherent and coherent error terms. Details of the error expressions are given in Appendix A. In this section we confine the discussion to general observations about the expected errors in  $\alpha_f$ ,  $\eta$ ,  $\tau_f$  and  $\tau_c$ .

[27] Figure 10 shows the total and derived optical parameters obtained by applying the spectral inversion algorithm to a simulated fine mode event where the input optical depth spectra were contaminated by normally distributed random noise vectors of 0.01 RMS amplitude in all 6 CIMEL channels employed in this study. The figure is useful because a number of error sources are illustrated. The amplitude of the errors in  $\alpha$  and  $\alpha'$  and the corresponding amplitude in the errors of the derived parameters vary as  $1/\tau_a$ . This can be observed in Figure 10 as a general decrease in the extent of the error clusters with increasing  $\tau_a$ . The second-order spectral polynomial fit applied to all  $\tau_a$  spectra forces a positive and negative correlation between the errors in  $\alpha$  and  $\tau_a$  and  $\alpha'$  and  $\tau_a$ , respectively. This correlation, which can be readily observed in the approximate linear behavior of the separate gray-toned clusters of Figure 10, is propagated through to the derived parameters and is the source of the coherent errors in the total error expressions given in Appendix A. Another artifact of the second-order polynomial fit (again propagated through to the derived parameters) is a negative bias in the estimated value of  $\alpha'$ . This is observable in the  $\alpha'$  versus  $\tau_a$  graph where the mean of each cluster of gray-toned points is less than the true  $\alpha'$  value (solid line).

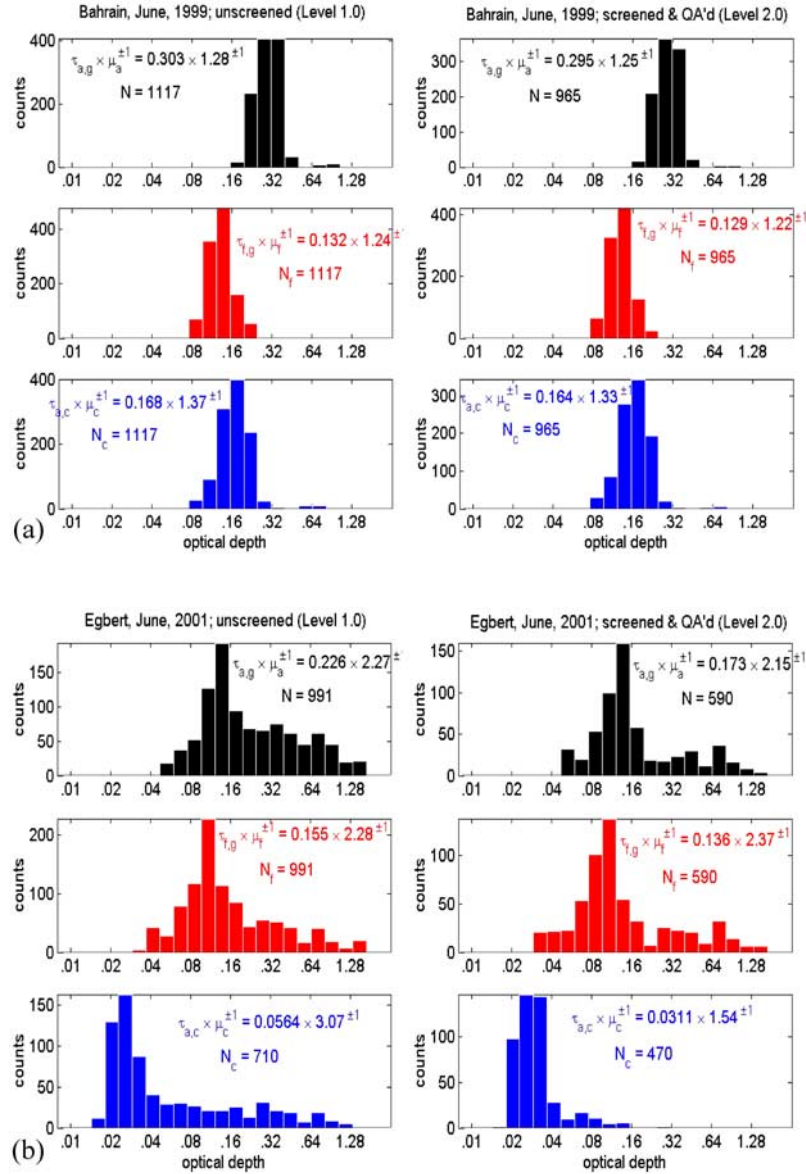


**Figure 9.** Histograms of  $\tau_a$ ,  $\tau_f$  and  $\tau_c$  resulting from the application of the spectral inversion algorithm to samples of monthly data. The left hand graphs in each of the four graphical pairs represent non cloud-screened data while the right hand graphs represent cloud-screened data.  $\tau_{g,x}$  and  $\mu_x$  refer to the geometric mean and standard deviation of the optical depth  $\tau_x$ . A logarithmic scale is employed for the optical depth axis. Color key: red, fine mode aerosol optical depth; blue, coarse mode aerosol optical depth; black, total aerosol optical depth. (a) Bahrain during the month of June 1999. (b) Egbert during the month of June 2001. (c) GSFC during the month of July 2002. (d) Nauru (South Pacific) for a period extending from 1 June 1999 to 31 May 2000.

[28] There are, in addition to measurement errors in  $\tau_a$ , errors due to the uncertainty in the assumed values of  $\alpha_c$  and  $\alpha'_c$  and the assumed relationship between  $\alpha'_f$  and  $\alpha_f$  [O'Neill *et al.*, 2001b]. The former errors are most critical in coarse mode dominated conditions ( $\eta \rightarrow 0$ ) near singularities in the factor  $1/(\alpha - \alpha_c)$ . An interesting illustration of sensitivity to  $\alpha'_c$  in coarse mode conditions occurred in the analysis of April 2001 dust events for the AERONET site at Dunhuang, China (near the dust source region). In this particular case, the presence of small positive  $\alpha'_f$  in thick dust atmospheres suggested that  $\alpha'_c \sim 0.25$  was closer to reality than the nominal value of  $\alpha'_c = 0$  assumed for other

sites ( $\alpha'_c \sim 0.25$  corresponds to unusually small coarse mode particles with an  $r_{\text{eff}} \sim 1 \mu\text{m}$ ). This inference was corroborated by significantly better analytical fits to the total optical parameters and by more realistic retrieved values of  $\alpha_f$ . At the same time the estimates of  $\tau_c$  were largely unaffected by the apparent disparity in the true value of  $\alpha'_c$  (the sensitivity to  $\alpha'_c$  was limited to  $\alpha_f$  and  $\tau_f$  which were at the limits of detectability).

[29] The coarse mode distribution is often bimodal rather than unimodal in appearance while the fine mode is typically a single, fairly symmetrical mode [see, e.g., Dubovik and King, 2002]. If the total PSD is accordingly trimodal



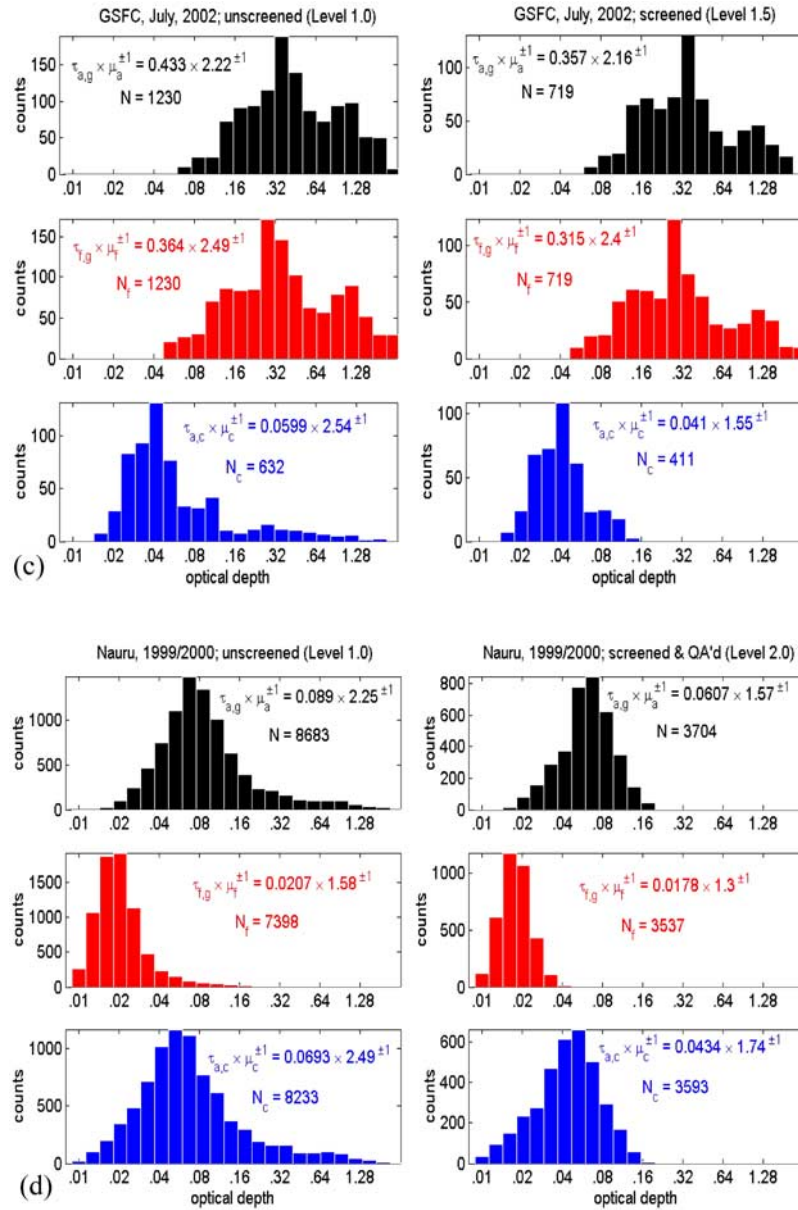


Figure 9. (continued)

then it is easy to show that the defining  $\alpha$  and  $\alpha'$  equations of O'Neill *et al.* [2000b] are unchanged provided one makes the substitutions below:

$$\alpha_c \leftrightarrow \langle \alpha_c \rangle \quad (2a)$$

$$\alpha'_c \leftrightarrow \langle \alpha'_c \rangle + \langle \alpha_c^2 \rangle - \langle \alpha'_c \rangle^2, \quad (2b)$$

where (the numerical subscripts referring to the smaller and larger of the coarse modes, respectively)

$$\tau_c = \tau_{c1} + \tau_{c2}, \quad \eta_c = \frac{\tau_{c1}}{\tau_c} \quad (3a)$$

$$\langle \alpha_c \rangle = (\eta_c \alpha_{c1} + (1 - \eta_c) \alpha_{c2}) \quad (3b)$$

$$\langle \alpha'_c \rangle = (\eta_c \alpha'_{c1} + (1 - \eta_c) \alpha'_{c2}). \quad (3c)$$

Various tests indicated that, unless the coarse mode is dominated by unusually small, near micron sized particles (c.f. the near-source dust case discussed above), these expressions yielded “equivalent” values of  $\alpha_c$  and  $\alpha'_c$  which were within the bounds of the assumed errors about the nominal values.

## 6. Conclusions

[30] The information content of solar extinction data resides in the magnitude and spectral variation of the aerosol optical depth. By assuming that the aerosol PSD is effectively bimodal one can exploit the spectral curvature information to extract the elemental optical parameters of each mode. PSD inversions of solar extinction and/or sky radiance data followed by a return to the optical domain provide a valuable source of information but an excess in intermediate detail if the goal is only to calculate  $\tau_f$  and  $\tau_c$ .

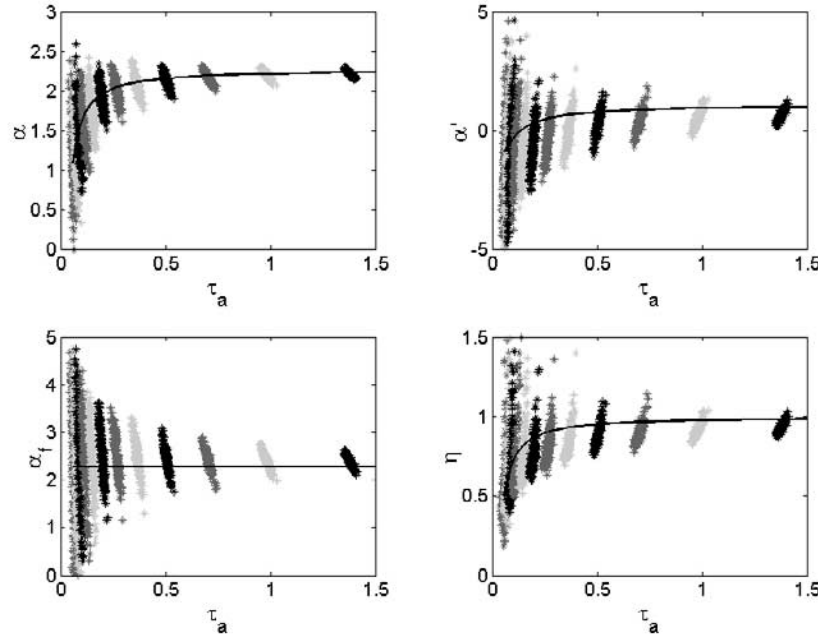


**Figure 10.** Illustration of a stochastic error simulation for  $\alpha_c$ ,  $\alpha'_c$ ,  $\alpha_f$  and  $\eta = \tau_f/\tau_a$ . Each cloud of gray-toned points represents computations for a nominal  $\tau_a$  spectra degraded by 200 random noise spectra with an RMS error of 0.01 in all bands. The solid curve represents true values.

The spectral curvature inversion yields a direct output which is commensurate in complexity with the information content of spectral extinction data and which is applicable to all extinction data rather than a limited database of combined extinction and sky radiance data as in the case of the formal PSD inversions.

[31] The extraction of  $\tau_f$  and  $\tau_c$  using the spectral curvature algorithm was partly validated by (1) demonstrating the physical consistency of the bimodal optical formulation and the component extractions, (2) demonstrating that  $\tau_c$  variation is coherent with photographic evidence of thin cloud events and that  $\tau_f$  variation is coherent with photographic evidence of clear sky and haze events and (3) by showing that the spectral curvature inversion technique yielded values of  $\tau_f$  and  $\tau_c$  which were well correlated if weakly biased relative to the values obtained from formal inversions of solar extinction and sky radiance data.

[32] Perturbations of monthly or longer-term statistical variations associated with passive or active shortcomings of operational cloud screening were inferred to be small to occasionally moderate over a sampling of cases. Diurnal illustrations were given where it was clear that such shortcomings can have a significant impact on the interpretation of specific events; (1) commission errors in  $\tau_f$  due to the exclusion of excessively high (temporal) frequency fine mode events and (2) omission errors in  $\tau_c$  due to the inclusion of insufficiently high (temporal) frequency, thin homogeneous cloud events.

[33] The separation of  $\tau_f$  and  $\tau_c$  is effectively a partial form of cloud screening which is applicable directly to non cloud-screened data (more precisely, it is a form of coarse mode discrimination where the coarse mode can

represent supermicron aerosols and/or cloud particles). The operational AERONET cloud-screening protocol fulfills its design criteria but does not discriminate between fine and coarse mode temporal excursions. The spectral curvature algorithm does discriminate between fine and coarse mode optical depths but cannot separate the optical effects of coarse mode aerosols from cloud particles.

[34] This represents a complementarity of information, which could be exploited in a hybrid (temporal and spectral) cloud-screening algorithm. In particular one could first apply the spectral curvature algorithm to separate  $\tau_f$  and  $\tau_c$  and subsequently apply a temporal exclusion algorithm to  $\tau_c$  (i.e., rather than  $\tau_a$ ) in order to separate the optical effects of coarse mode aerosols from those of cloud particles. Such an algorithm would eliminate the unnecessary exclusion of high-frequency  $\tau_f$  variations and would be more attuned to cloud optical depth variations since the temporal constraints would be appropriately focused on  $\tau_c$ .

## Appendix A: Error Model

### A1. General Error Expression

[35] The errors in the parameters derived from the spectral curvature algorithm can be expressed as

$$\Delta\alpha_f^2 = \left( k_1 \frac{\partial\alpha_f}{\partial\alpha'} + k_2 \frac{\partial\alpha_f}{\partial\alpha} \right)^2 \left( \frac{\Delta\tau_a}{\tau_a} \right)^2 + \left( \frac{\partial\alpha_f}{\partial\alpha'} \Delta\alpha'_f \right)^2 + \left( \frac{\partial\alpha_f}{\partial\alpha'} \Delta\alpha'_c \right)^2 + \left( \frac{\partial\alpha_f}{\partial\alpha} \Delta\alpha_c \right)^2 \quad (A1)$$

$$\left(\frac{\Delta\tau_f}{\tau_a}\right)^2 = \left(k_1 \frac{\partial\eta}{\partial\alpha'} + k_2 \frac{\partial\eta}{\partial\alpha} + \eta\right)^2 \left(\frac{\Delta\tau_a}{\tau_a}\right)^2 + \left(\frac{\partial\eta}{\partial\alpha'_f} \Delta\alpha'_f\right)^2 + \left(\frac{\partial\eta}{\partial\alpha'_c} \Delta\alpha'_c\right)^2 + \left(\frac{\partial\eta}{\partial\alpha_c} \Delta\alpha_c\right)^2 \quad (\text{A2})$$

$$\left(\frac{\Delta\tau_c}{\tau_a}\right)^2 = \left(1 - k_1 \frac{\partial\eta}{\partial\alpha'} - k_2 \frac{\partial\eta}{\partial\alpha} - \eta\right)^2 \left(\frac{\Delta\tau_a}{\tau_a}\right)^2 + \left(\frac{\partial\eta}{\partial\alpha'_f} \Delta\alpha'_f\right)^2 + \left(\frac{\partial\eta}{\partial\alpha'_c} \Delta\alpha'_c\right)^2 + \left(\frac{\partial\eta}{\partial\alpha_c} \Delta\alpha_c\right)^2, \quad (\text{A3})$$

where coherent terms except those involving  $\Delta\alpha$  and  $\Delta\alpha'$  have been discarded. The averaging of this expression over an ensemble of measurements means that we replace the input errors ( $\Delta\tau_a$  etc.) by estimates of their mean square averages. Stochastic error simulations over a number of representative fine and coarse mode cases (of which Figure 10 is an illustration) yielded the empirical relationships;  $\Delta\alpha \sim -2.5 \Delta\tau_a/\tau_a = k_2 \Delta\tau_a/\tau_a$  and  $\Delta\alpha' \sim k_1 \Delta\tau_a/\tau_a$  where  $k_1 \sim 10 + 10 \exp[-\{(\alpha - 2)/(0.75\sqrt{2})\}^2]$  if  $\alpha < 2$  and 20 otherwise. The partial derivative expressions are given in the sections that follow. Input values of the dependent RMS error vectors were taken as  $\{\Delta\alpha, \Delta\alpha', \Delta\alpha'_f, \Delta\alpha'_c, \Delta\alpha_c, \Delta\alpha'_c\}_{\text{rms}} = \{k_2 \Delta\tau_a/\tau_a, k_1 \Delta\tau_a/\tau_a, 0.5, 0.15, 0.15\}$ .

[36] The negative  $\alpha'$  bias error introduced in the error estimation section is a function of the difference between the average of  $\alpha'$  over the range of CIMEL wavelengths less  $\alpha'$  at 500 nm. The (positive)  $\alpha'$  bias correction was coarsely approximated by the following function of  $\eta$ :

$$\Delta\alpha'_{\text{bias}} = 0.65 \exp\left[-(\eta - .78)^2 / (2 \times 0.18^2)\right].$$

This small correction is added to the computed value of  $\alpha'$  and propagated through all computations to yield a bias corrected set of outputs (all results in this paper were bias corrected).

## A2. Partial Derivatives of $\alpha_f$

[37] The general expression for  $\alpha_f$  from *O'Neill et al.* [2001b] is

$$\alpha_f - \alpha_c = \frac{1}{2(1-a)} \{t + b^* + D\},$$

where

$$D = \sqrt{(t + b^*)^2 + 4(1-a)c^*}$$

$$b^* = b + 2\alpha_c a, c^* = c + (b + a\alpha_c)\alpha_c - \alpha'_c,$$

and

$$t = \alpha - \alpha_c - \frac{\alpha' - \alpha'_c}{\alpha - \alpha_c}.$$

From the above expressions,

$$\frac{\partial t}{\partial \alpha} = 1 + \frac{\alpha' - \alpha'_c}{(\alpha - \alpha_c)^2} = \frac{t_+}{\alpha - \alpha_c},$$

where

$$t_+ = \alpha - \alpha_c + \frac{\alpha' - \alpha'_c}{\alpha - \alpha_c} \frac{\partial D}{\partial \alpha} = \frac{1}{2} \frac{1}{D} 2(t + b^*) \frac{\partial t}{\partial \alpha} = \frac{(t + b^*)}{D} \frac{t_+}{\alpha - \alpha_c},$$

so that

$$\begin{aligned} \frac{\partial \alpha_f}{\partial \alpha} &= \frac{1}{2(1-a)} \left( \frac{\partial t}{\partial \alpha} + \frac{\partial D}{\partial \alpha} \right) \\ &= \frac{1}{2(1-a)} \frac{t_+}{\alpha - \alpha_c} \left( 1 + \frac{(t + b^*)}{D} \right) \\ &= \frac{\alpha_f - \alpha_c}{\alpha - \alpha_c} \frac{t_+}{D} = \frac{t_+}{\eta D}. \end{aligned}$$

Similarly,

$$\begin{aligned} \frac{\partial \alpha_f}{\partial \alpha'} &= \frac{-1}{\alpha - \alpha_c} \\ \frac{\partial D}{\partial \alpha'} &= \frac{1}{2} \frac{1}{D} 2(t + b^*) \frac{\partial t}{\partial \alpha'} = -\frac{(t + b^*)}{D} \frac{1}{\alpha - \alpha_c}, \end{aligned}$$

so that

$$\begin{aligned} \frac{\partial \alpha_f}{\partial \alpha'} &= \frac{1}{2(1-a)} \left( \frac{\partial t}{\partial \alpha'} + \frac{\partial D}{\partial \alpha'} \right) = \frac{1}{2(1-a)} \frac{-1}{\alpha - \alpha_c} \left( 1 + \frac{(t + b^*)}{D} \right) \\ &= \frac{\alpha_f - \alpha_c}{\alpha - \alpha_c} \left( \frac{-1}{D} \right) = \frac{-1}{\eta D}. \end{aligned}$$

We next seek the partial derivatives relative to the coarse mode parameters:

$$\frac{\partial \alpha_f}{\partial \alpha_c} = 1 + \frac{1}{2(1-a)} \left\{ \frac{\partial t}{\partial \alpha_c} + \frac{\partial b^*}{\partial \alpha_c} + \frac{\partial D}{\partial \alpha_c} \right\},$$

where

$$\frac{\partial t}{\partial \alpha_c} = \frac{\alpha' - \alpha'_c}{(\alpha - \alpha_c)^2}, \frac{\partial b^*}{\partial \alpha_c} = 2a, \frac{\partial c^*}{\partial \alpha_c} = 2a\alpha_c,$$

and

$$\frac{\partial D}{\partial \alpha_c} = \frac{1}{D} \left[ (t + b^*) \left( \frac{\partial t}{\partial \alpha_c} + 2a \right) + 4(1-a)a\alpha_c \right].$$

Also,

$$\frac{\partial \alpha_f}{\partial \alpha'_c} = \frac{1}{2(1-a)} \left\{ \frac{\partial t}{\partial \alpha'_c} + \frac{\partial D}{\partial \alpha'_c} \right\},$$

where

$$\frac{\partial t}{\partial \alpha'_c} = \frac{1}{\alpha - \alpha_c},$$

and

$$\frac{\partial D}{\partial \alpha'_c} = \frac{1}{2} \frac{1}{D} \left[ 2(t + b^*) \frac{\partial t}{\partial \alpha'_c} + 4(1-a) \frac{\partial c^*}{\partial \alpha'_c} \right], \frac{\partial c^*}{\partial \alpha'_c} = -1.$$

If we directly employ the expression in terms of  $\alpha'_f$ ,

$$\alpha_f - \alpha_c = \frac{1}{2} \left\{ t + \sqrt{t^2 + 4(\alpha'_f - \alpha'_c)} \right\},$$

then

$$\frac{\partial \alpha_f}{\partial \alpha'_f} = \frac{1}{2} \frac{1}{\sqrt{t^2 + 4(\alpha'_f - \alpha'_c)}} = \frac{1}{\sqrt{t^2 + 4(\alpha'_f - \alpha'_c)}}.$$

### A3. Partial Derivatives of $\eta$

[38] The differential in  $\eta$  is derived from the fundamental expression

$$\begin{aligned} \eta &= \frac{\alpha_f - \alpha_c}{\alpha_f - \alpha_c} \\ d\eta &= \frac{1}{\alpha_f - \alpha_c} (\Delta\alpha - \eta\Delta\alpha_f - (1 - \eta)\Delta\alpha_c) \\ d\eta &= \frac{1}{\alpha_f - \alpha_c} \left( \Delta\alpha - \eta \left\{ \frac{\partial \alpha_f}{\partial \alpha'} \Delta\alpha' + \frac{\partial \alpha_f}{\partial \alpha} \Delta\alpha \right\} \right. \\ &\quad \left. + \frac{\partial \alpha_f}{\partial \alpha'_f} \Delta\alpha'_f + \frac{\partial \alpha_f}{\partial \alpha'_c} \Delta\alpha'_c + \frac{\partial \alpha_f}{\partial \alpha_c} \Delta\alpha_c \right) - (1 - \eta)\Delta\alpha_c \\ &= \frac{1}{\alpha_f - \alpha_c} \left( \left( 1 - \eta \frac{\partial \alpha_f}{\partial \alpha} \right) \Delta\alpha - \eta \frac{\partial \alpha_f}{\partial \alpha'} \Delta\alpha' \right. \\ &\quad \left. - \eta \frac{\partial \alpha_f}{\partial \alpha'_f} \Delta\alpha'_f - \eta \frac{\partial \alpha_f}{\partial \alpha'_c} \Delta\alpha'_c - \left( 1 - \eta + \eta \frac{\partial \alpha_f}{\partial \alpha_c} \right) \Delta\alpha_c \right). \end{aligned}$$

From the above expression the partial derivatives of  $\eta$  are given by

$$\begin{aligned} \frac{\partial \eta}{\partial \alpha} &= \frac{1 - \eta \frac{\partial \alpha_f}{\partial \alpha}}{\alpha_f - \alpha_c} \\ \frac{\partial \eta}{\partial \alpha'} &= \frac{-\eta \frac{\partial \alpha_f}{\partial \alpha'}}{\alpha_f - \alpha_c}, \\ \frac{\partial \eta}{\partial \alpha'_f} &= \frac{-\eta \frac{\partial \alpha_f}{\partial \alpha'_f}}{\alpha_f - \alpha_c}, \quad \frac{\partial \eta}{\partial \alpha'_c} = \frac{-\eta \frac{\partial \alpha_f}{\partial \alpha'_c}}{\alpha_f - \alpha_c}, \quad \frac{\partial \eta}{\partial \alpha_c} = \frac{-\left( 1 - \eta + \eta \frac{\partial \alpha_f}{\partial \alpha_c} \right)}{\alpha_f - \alpha_c}. \end{aligned}$$

### Notation

$\alpha_f$	instantaneous slope of $-\ln \tau_f$ versus $\ln \lambda$ .
$\alpha_c$	instantaneous slope of $-\ln \tau_c$ versus $\ln \lambda$ .
$\alpha$	instantaneous slope of $\ln \tau_a$ versus $\ln \lambda$ ; $\alpha = \alpha_f \eta + (1 - \eta)\alpha_c$ .
$\alpha'_f$	instantaneous slope of $\alpha_f$ versus $\ln \lambda$ .
$\alpha'_c$	instantaneous slope of $\alpha_c$ versus $\ln \lambda$ .
$\alpha'$	instantaneous slope of $\alpha$ versus $\ln \lambda$ .
$\eta$	optical mixing ratio $\eta = \tau_f/\tau_a$ .
$\tau_a$	total aerosol optical depth; $\tau_a = \tau_f + \tau_c$ .
$\tau_c$	coarse mode optical depth $\tau_c = \tau_{c,aerosol} + \tau_{cloud}$ .
$\tau_{cloud}$	cloud optical depth.
$\tau_f$	fine mode optical depth.

$\tau_{g,x}$  geometric mean associated with a lognormal frequency distribution. If  $\langle \log \tau_x \rangle$  is the mean of a  $\tau_x$  distribution on a log scale then  $\tau_{g,x} = 10^{\langle \log \tau_x \rangle}$ .  
 $\mu_x$  geometric standard deviation associated with a lognormal frequency distribution. If  $\sigma(\log \tau_x)$  is the standard deviation of a  $\tau_x$  distribution on a log scale then  $\mu_x = 10^{\sigma(\log \tau_x)}$ .

[39] All optical quantities referenced to 500 nm wavelength, and all parameters are unitless.

[40] **Acknowledgments.** The authors would like to thank NASA, the National Sciences and Engineering Research Council of Canada (NSERC), and the Canadian Foundation for Climate and Atmospheric Sciences (CFCAS) for their financial support. Valuable in-kind support was obtained from the Canada Center for Remote Sensing (CCRS) and the Meteorological Services of Canada (MSC). Discussions with Oleg Dubovik of the AERONET group were very useful and much appreciated. The contributions of Ilya Slutsker of the AERONET group, Alain Royer, the co-PI of the AEROCAN network, and Jim Freemantle, the AEROCAN coordinator and the Egbert PI, are gratefully acknowledged. The southern Great Plains data were obtained from the Atmospheric Radiation Measurement (ARM) Program sponsored by the U.S. Department of Energy, Office of Science, Office of Biological and Environmental Research, Environmental Sciences Division. We are also grateful to Frank Froude, the Egbert instrumentation manager, for his sky camera data.

### References

- Dubovik, O., and M. D. King, A flexible inversion algorithm for retrieval of aerosol optical properties from Sun and sky radiance measurements, *J. Geophys. Res.*, **105**, 20,673–20,696, 2000.
- Dubovik, O., B. N. Holben, T. F. Eck, A. Smirnov, Y. J. Kaufman, M. D. King, D. Tanré, and I. Slutsker, Variability of absorption and optical properties of key aerosol types observed in worldwide locations, *J. Atmos. Sci.*, **59**, 590–608, 2002.
- Eck, T. F., B. N. Holben, J. S. Reid, O. Dubovik, A. Smirnov, N. T. O'Neill, I. Slutsker, and S. Kinne, The wavelength dependence of the optical depth of biomass burning, urban and desert dust aerosols, *J. Geophys. Res.*, **104**, 31,333–31,350, 1999.
- Holben, B. N., et al., AERONET—A federated instrument network and data archive for aerosol characterization, *Remote Sens. Environ.*, **66**, 1–16, 1998.
- Kent, G. S., M. P. McCormick, and P.-H. Wang, Validation of Stratospheric and Gas Experiments I and II satellite optical depth measurements using surface radiometer data, *J. Geophys. Res.*, **99**, 10,333–10,339, 1994.
- Kinne, S., T. P. Akerman, M. Shiobara, A. Uchiyama, A. J. Heymsfield, L. Miloshevich, J. Wendell, E. W. Eloranta, C. Purgold, and R. W. Bergstrom, Cirrus cloud radiative and microphysical properties from ground observations an in situ measurements during FIRE 1991 and their application to exhibit problems in cirrus solar radiative transfer modelling, *J. Atmos. Sci.*, **54**, 2320–2344, 1997.
- O'Neill, N. T., T. F. Eck, B. N. Holben, A. Smirnov, O. Dubovik, and A. Royer, Bimodal size distribution influences on the variation of Angstrom derivatives in spectral and optical depth space, *J. Geophys. Res.*, **106**, 9787–9806, 2001a.
- O'Neill, N. T., O. Dubovik, and T. F. Eck, A modified Angstrom coefficient for the characterization of sub-micron aerosols, *App. Opt.*, **40**(14), 2368–2375, 2001b.
- Smirnov, A., B. N. Holben, T. F. Eck, O. Dubovik, and I. Slutsker, Cloud screening and quality control algorithms for the AERONET data base, *Remote Sens. Environ.*, **73**, 337–349, 2000.
- Smirnov, A., B. N. Holben, Y. J. Kaufman, O. Dubovik, T. F. Eck, I. Slutsker, C. Pietras, and R. Halthore, Optical properties of atmospheric aerosol in maritime environments, *J. Atmos. Sci.*, **59**, 501–523, 2002.
- Tanré, D., L. A. Remer, Y. J. Kaufman, S. Mattoo, P. V. Hobbs, J. M. Livingstone, P. B. Russell, and A. Smirnov, Retrieval of aerosol optical thickness and size distribution over ocean from the MODIS airborne simulator during TARFOX, *J. Geophys. Res.*, **104**(D2), 2261–2278, 1999.
- T. Eck, B. N. Holben, and A. Smirnov, NASA Goddard Space Flight Center, RSTX Code 923, Greenbelt, MD 20771, USA. (teck@ltpmail.gsfc.nasa.gov; brent@aeronet.gsfc.nasa.gov; asmirnov@ltpmail.gsfc.nasa.gov)
- N. T. O'Neill and S. Thulasiraman, CARTEL, Université de Sherbrooke, 2500 Bd. de l'Université, Sherbrooke, Quebec J1K 2R1, Canada. (noneill@courrier.usherb.ca; Thulasiraman.Srinivasan@Usherbrooke.Ca)